Progress In Electromagnetics Research B, Vol. 61, 169–184, 2014

Three-Dimensional Far-Field Holographic Microwave Imaging: An Experimental Investigation of Dielectric Object

Lulu Wang[1, *], Ray Simpkin[2], and Ahmed M. Al-Jumaily[1]

Abstract—This work presents experimental investigations of three-dimensional (3-D) far-field holographic microwave imaging (HMI) method for diagnosing inclusions within dielectric objects, and in particular, it relates to electromagnetic imaging to reconstruct dielectric properties of inhomogeneous, lossy bodies with arbitrary shape. The apparatus is designed for operation at a single frequency of 12.6 GHz. 16 antennas are located on a 2-D array plane which is placed under the object in the far-field region, with air in the space between the antenna array and the object. Experimental results indicate that the 3-D HMI system has the ability to produce a 3-D image of multimedia dielectric object and detect small inclusions embedded within an object. The invention has potential application to tissue imaging.

1. INTRODUCTION

Microwave imaging techniques are used to probe inaccessible domains and to reveal the dielectric properties of the media that they penetrate [1]. Microwave imaging based techniques have found a variety of applications such as medical diagnosis [2, 3], concealed weapon detection [4], food and agricultural applications [1].

Several microwave imaging techniques with a particular focus on breast cancer detection have been investigated by a number of research groups [5–9], which include radar-based, tomography and microwave holography method. The physical basis for microwave breast imaging is tissue dependent microwave scattering and absorption in the breast due to the contrast in the dielectric properties between the malignant and normal breast tissues [10]. Additional factors to support microwave breast imaging are that microwave signals attenuate significantly less (about 4 dB/cm) in healthy tissue, and breasts naturally protrude outside the human body.

Radar-based techniques [11, 12] detect strongly scattering tumours using measurements of energy reflected from the breast. Tomography [13–17] reconstructs a map of the electrical properties in the breast using measurements of energy transmitted through the breast. Microwave holographic based techniques [18–21] do not require expensive ultra-high speed electronics as narrow-band signals can be converted to the baseband for digitization at a slower rate, thereby enabling imaging at significantly lower cost [22]. Microwave holographic methods use both magnitude and phase information in an inversion process, which reconstructs the target reflectivity as a function of position [23].

However, there are various limitations in existing microwave imaging techniques. Recent extensive measurements on the dielectric properties of different types of breast tissues discovered that the dielectric contrast varies widely from individual to individual, with age and other biological factors [24–28]. The limited resolution comes from the fact that the heterogeneous structure of the breast causes multiple scatterings and reflections of the microwave signal while penetrating inside the different types of tissues [29].

Received 15 October 2014, Accepted 10 November 2014, Scheduled 18 November 2014

* Corresponding author: Lulu Wang (luwang@aut.ac.nz).

[1] Institute of Biomedical Technologies, AUT University, Auckland, New Zealand. [2] Callaghan Innovation, Auckland, New Zealand.

We propose a new microwave imaging technique which has a potential for tissue imaging with particular focus on breast cancer detection and brain stroke detection [30–32]. We call this technique 2-D far-filed holographic microwave imaging array (HMIA) technique. However, this technique has one major limitation of missing detection small lesions if more than one lesion is located at the same x and y coordinates but at different z-planes. To overcome this limitation, we developed 3-D HMI imaging method [33–35].

The main object of this invention was to provide a new 3-D holographic microwave imaging technique for reconstructing the dielectric properties of inhomogeneous, lossy bodies with arbitrary shape. Another object of the invention was to provide a data acquisition system to validate the proposed imaging method. This paper reports the experimental validation of the 3-D HMI method using simple objects embedded in a host medium. Whilst not fully representative of human tissue, the objects chosen for experimental study were deemed to be suitable for testing the validity of the imaging technique in the first instance.

The remainder of the paper is organized as follows. In Section 2, the 3-D HMI apparatus is introduced. System setup and experimental measurements on various objects are given in Section 3. In Section 4, signal processing and imaging algorithm are presented; experimental results and conclusions are detailed in Sections 5 and 6, respectively.

2. 3-D HOLOGRAPHIC MICROWAVE IMAGING

A possible implementation of a 3-D HMI system is shown in Figure 1. A dielectric object (not showing) is placed on the window of an examination bed. Referring to Figure 1(b), the proposed system consists of an array of 16 small microwave antennas with one of the elements being the transmitter and the other being the receivers. All antennas are located on the 2-D antenna array plane, which are connected to a 16-channel switch. The antenna array plane is placed under the examination bed in the far-field region of the array ($> 6\lambda$) and it is designed to be moveable towards the target object in a vertical position so that measurements can be performed at different distances between the object and array plane. The space between the examination window and the antenna array plane is filled with host medium. During operation, one port of a microwave generator excites the single transmitter at one frequency of 12.6 GHz. The magnitude and phase of the back-scattered electric field from the target object is measured at each receiver element in the array plane, which is connected to the second port of the microwave generator via a 16-channel switch. These measurements are repeated for every new

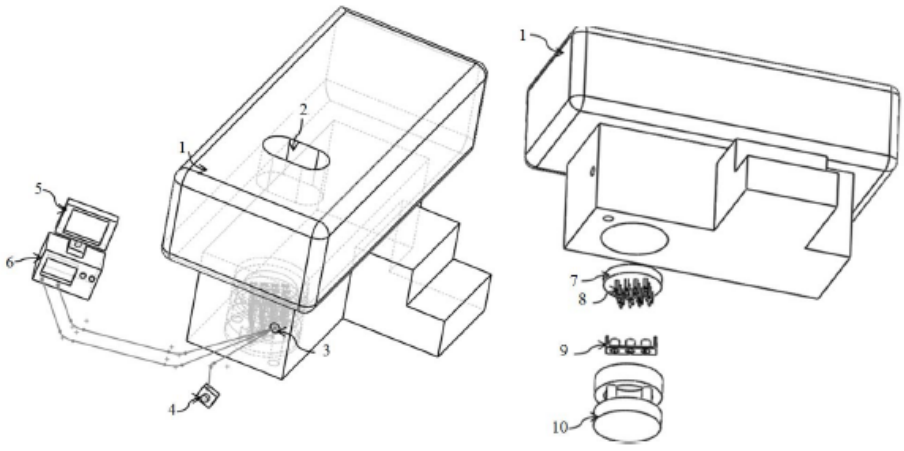

Figure 1. (a) 3-D holographic microwave imaging system, (b) bottom view of examination bed (1: examination bed, 2: examination window, 3: connection hole to antennas, 4: multi-position switch, 5: computer, 6: microwave generator, 7: antenna array plane, 8: antennas, 9: multi-position switch assembly, 10: antenna array holder).

vertical position of the antenna array plane. It will be shown in the following section that the complex valued data measured at each receiving antenna can be used to calculate the complex visibility function for each possible pair of antennas. This function can then be used to form a 2-D image using an inverse Fourier transform. A 3-D image is then reconstructed from a sequence of 2-D images obtained at each vertical position of the antenna array.

A computer with MATLAB software is used to analyse the reflected singles and perform 3-D image of the object under test by using the developed 3-D HMI imaging algorithm. The development of HMI imaging algorithms and numerical simulation investigations are reported in [30–37].

3. EXPERIMENTAL METHOD

3.1. Model and Materials

In order to test the performance of the 3-D HMI technique, a dielectric object was used to verify the main characteristics of the system such as contrast, spatial resolution, size and positioning accuracy.

The cube-shaped dielectric object consisted of an external cube made from an embedding medium and an inclusion. The external cube I was made from emulsifying ointment that contained 30% emulsifying wax, 50% white soft paraffin and 20% liquid paraffin. The external cube II was made of 90% emulsifying ointment and 10% water.

Small grapes (7 mm to 15 mm in diameter) were inserted into the cube object to represent inclusion I. A small blueberry (9 mm in diameter) was inserted into the cube object to represent inclusion II.

The dielectric object was covered by a thin plastic film to minimize moisture loss and to make the object easier to handle. The plastic film has a negligible effect on the scattered electromagnetic field in the considered frequency range. Air ($\varepsilon_r = 1$) was used as the medium filling the space between the dielectric object and antenna array.

3.2. Dielectric Properties Measurement

The actual dielectric properties of the external cube and inclusion were measured before 3-D HMI data collection. Measurements with frequencies ranging from 10 GHz to 20 GHz were conducted using Agilent N5230APNA and an Agilent 85070 single port dielectric probe. Reflection coefficients were converted to dielectric permittivity and loss tangent using Agilent 85070 dielectric measurement software.

A dielectric kit open-ended coaxial probe was connected to the network analyser for calibration. Probe calibration was carried out using three calibration standards: air, short-circuit and finally deionized water at a temperature of 21°C.

Following calibration, the probe was pressed against the sample ensuring no air gaps between sample and probe. The reflection coefficient was measured and used to determine the permittivity. Data was recorded at 101 frequency points between 10 GHz to 20 GHz. This measurement was repeated three times in order to get an average reading. The sample must be thick enough to appear effectively

Table 1. Dielectric properties of materials at 12.6 GHz.

Material	Real part of permittivity	Imaginary part of permittivity	Size (mm)
External cube I (100% wax)	2.43	0.24	180 by 160 by 40; 100 by 100 by 30; 100 by 100 by 30
External cube II (90% wax and 10% water)	3.16	0.53	100 by 100 by 40
Inclusion I (Grape)	21.23	19.3	Diameters: 4, 5, 7, 10, 15
Inclusion II (Blueberry)	27.73	7.98	Diameter: 9

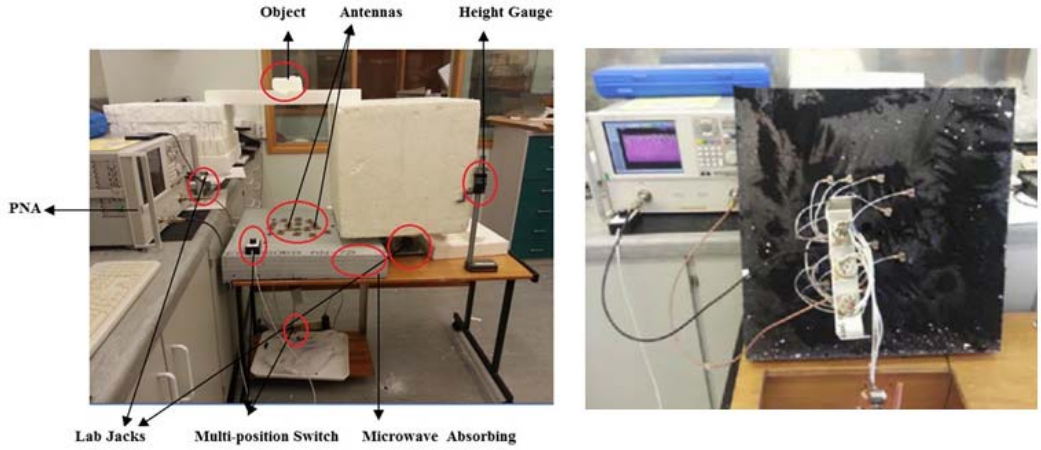

Figure 2. (a) Photo of 3D HMI system experimental set-up. (b) Bottom view of antenna array plane.

semi-infinite to the probe. After measuring each object, the probe was cleaned with tissue paper to prevent any oil that may accumulate on it during measurements. The measured dielectric properties at 12.6 GHz ($\lambda = 23.8$ mm) of the external cube and inclusion are listed in Table 1.

3.3. Experimental System Setup

Figure 2 shows the photograph of our initial 3-D HMI data acquisition system. An array of 16 open-ended rectangular wave-guide antennas was surrounded with ECCOSORB AN79 (600 mm by 600 mm) electromagnetic absorbing material to reduce ambient reflections and coupling noise between each two antennas, and antennas were positioned as shown in Figure 3. Optimization of the antenna array configuration to produce high-resolution images was documented in [36].

A small open-ended rectangular wave-guide antenna was selected as a transmitter and receiver in all experiments because of its low-cost and ease of manufacture. The antenna array was connected to an Agilent N5230A (10 MHz–20 GHz) PNA. The target object was placed on the top of the polystyrene box bridge. Two lab jacks were used to adjust the vertical distance between the antenna array plane and the target object. The target object was located at a height above the antenna array plane that was varied between $z = 540$ mm (22.7λ) to $z = 550$ mm (23λ) in 11 equal steps by adjusting two lab jacks.

A height gauge was used to measure the target object movements of 1 mm increments and a spirit level was used to balance the polystyrene box bridge during movement.

3.4. Data Acquisition

Although only a single frequency was used for reconstructing the image, the wide frequency spectrum from 10 GHz to 20 GHz was collected so that the optimal frequency could be determined. Data was recorded at 3201 frequency points for choosing the optimum frequency between 10 GHz to 20 GHz and 101 measurements were averaged at each frequency. All 16 antennas were tested before data acquisition with one antenna as the transmitter and the 15 others as the receivers.

Background data (that is, with no object present) was collected at each receiver with the antenna array plane placed at $z = 540$ mm (22.7λ) before measuring the target object. This step was repeated three times and the data averaged.

The dielectric object was illuminated by the transmitter and the backscattered field recorded at each receiver at the operating frequency of 12.6 GHz ($\lambda = 23.8$ mm)for all receivers located on the antenna array plane. These data collection steps were repeated for every new vertical position of the antenna array.

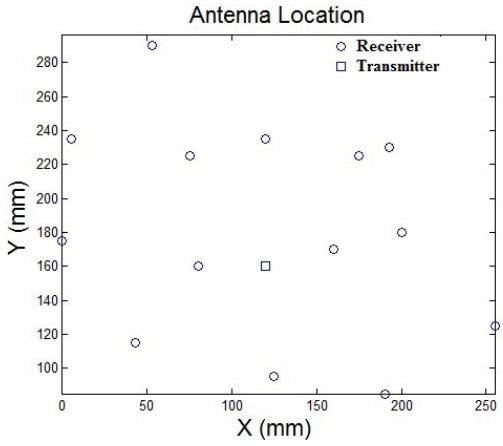

Figure 3. Schematic diagram of antenna array configuration.

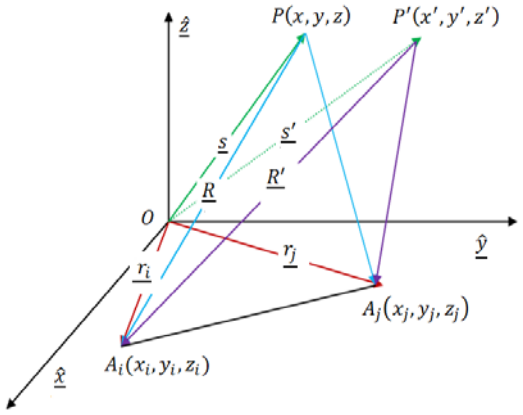

Figure 4. Geometry of HMI measurement by a pair of antennas.

4. SIGNAL AND IMAGING PROCESSING

4.1. Imaging Processing

Figure 4 shows the invention configuration for a given pair of receiving antenna elements. The point $P(x, y, z)$ defines a point within the interior of the object under test. Under far-field conditions, the complex visibility function, G, of the back-scattered electric field, $\underline{E}_{scat}$, for any two receiving antennas located at $\underline{r_i}$ and $\underline{r_j}$ is defined as [38]:

$$G\left(\underline{r_i}, \underline{r_j}\right) = \left\langle \underline{E}_{scat}\left(\underline{r_i}\right) \cdot \underline{E}^*_{scat}\left(\underline{r_j}\right) \right\rangle \tag{1}$$

where asterisk in (1) denotes the complex conjugate and $\langle\,\rangle$ represents the time average.

It is well known that the scattered electric field can be represented as an integral over the volume of the scatterer involving the induced polarization currents that arise from the complex permittivity contrast with respect to the ambient medium (which in this case is air). For far-field conditions, the scattered field at any receiver can be represented by the following volume integral:

$$\underline{E}_{scat} = \frac{k_0^2}{4\pi} \int_V \left(\varepsilon\left(\underline{s}\right) - \varepsilon_1\right) \underline{E}_{tot}\left(\underline{s}\right) \frac{e^{-jk_0|\underline{s}-\underline{r}|}}{|\underline{s}-\underline{r}|} dV \tag{2}$$

where k_0 = Free-space propagation;
$\varepsilon(\underline{s})$ = Complex relative permittivity distribution inside the dielectric object;
ε_1 = Relative permittivity of the host medium;
$j = \sqrt{-1}$;
$E_{tot}(\underline{s})$ = Total electric field at a point inside the object with position vector, $\underline{s}$;
$\underline{r}$ = Position vector from a point in the dielectric inside the dielectric object.

The intensity distribution of an object, $I(\underline{s})$, at position $\underline{s}$ is defined as [30]:

$$I\left(\underline{s}\right) = \left(\frac{k_0^2}{4\pi}\right)^2 \left|\varepsilon\left(\underline{s}\right) - \varepsilon_1\right|^2 \underline{E}_{tot}(\underline{s}) \cdot \underline{E}^*_{tot}(\underline{s}') \tag{3}$$

The quantity that we reconstruct at each voxel is that defined in (3), which we simply refer to as 'intensity'. Physically, this quantity is proportional to the squared modulus of the polarisation charge density at each point inside the object. Note that this is a scalar quantity, which simplifies the image reconstruction.

Writing the Cartesian components of the baseline vector $\underline{D}$ as (u, v, w) such that:

$$u = \left(\underline{x_j} - \underline{x_i}\right)/\lambda_1; \quad v = \left(\underline{y_j} - \underline{y_i}\right)/\lambda_1; \quad w = \left(\underline{z_j} - \underline{z_i}\right)/\lambda_1 \tag{4}$$

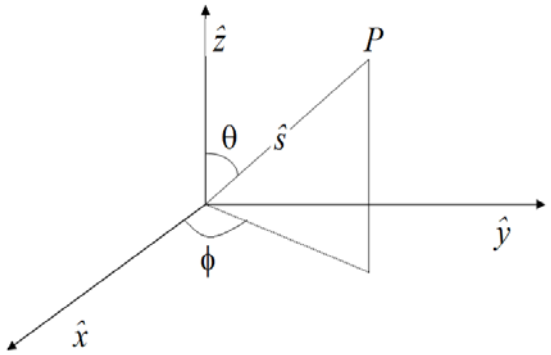

Figure 5. Spherical polar coordinate system.

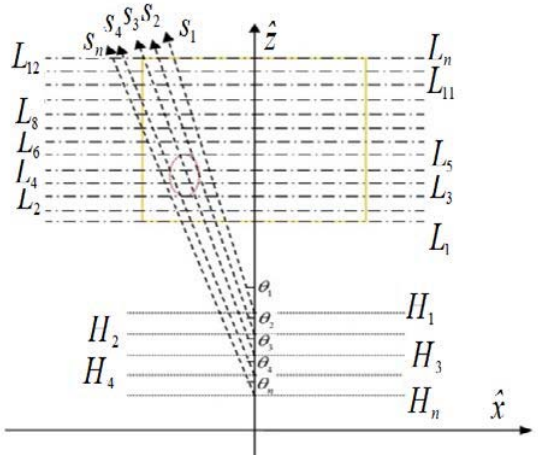

Figure 6. Block diagram showing the scattering characterization scheme from different receiving height H_n.

where λ_1 indicates the wavelength in the host medium (air in this study).

As all antennas are located on a 2-D flat plane, then the 2-D intensity function of the object under test obtained by Fourier inversion is:

$$\tilde{I}(l,m) = \iint G(u,v,w=0)\, e^{j2\pi(ul+vm)} dldm \tag{5}$$

where $l = \sin\theta\cos\phi$ and $m = \sin\theta\sin\phi$ in Equation (4) (refers to Figure 5). The 2-D image is the intensity function $\tilde{I}(lm)$, it is a projection of the 3-D intensity function $I(s, l, m)$ onto a 2-D plane in (l, m) space.

In order to obtain a 3-D image, the antenna array plane was designed to be movable along the z-axis from H_1 to H_n in M equal steps, where H in Figure 6 is the vertical distance between the antenna array plane and the target object. By differentiating intensity function with respect to s, the 3-D intensity function at a selected height $H = H_n$ can be obtained as:

$$I(H = z_n, l, m) = \frac{d\tilde{I}(l,m) \cdot \left(1 - l^2 - m^2\right)}{dz} \tag{6}$$

The derivative in (6) can be approximated by the following forward difference expression:

$$\frac{d\tilde{I}}{dz} = \frac{\tilde{I}_{Z_n} - \tilde{I}_{Z_{n-1}}}{Z_n - Z_{n-1}} \tag{7}$$

The complex visibility function can be computed using (1) for all possible pairs of receiving antennas, with the background scattered field subtracted from the data. For example, for N receivers, the measured complex visibility data is $N(N-1)$. Referring to Equations (1) and (4), a 2-D image can be reconstructed using complex visibility data that is collected when the antenna array plane is placed at the selected height.

A reconstructed 3-D image of the object is then computed using (6) and (7) by acquiring measured data with the antenna array placed at different heights, and computing the sequence of 2-D images, $\tilde{I}_{Z_n}$. The development of 3-D HMI imaging algorithm was documented in [33].

4.2. Calibration

The measured signals include direct coupling between the antennas and reflections from the target object, therefore calibration is necessary to remove coupling noise. In this study, the calibration signal was the average of background measurements, that is, with no test object present. This measured signal was subtracted from the actual response recorded for the target object at each receiving antenna. This step was repeated for every new vertical position of the antenna array. The antenna coupling signal was obtained both without the target object present in the measurement (background) and with the image.

5. IMAGING RESULTS AND DISCUSS

5.1. Reconstruction Results

Figure 7 shows the dielectric object consisting of external cube I (180 mm by 160 mm by 40 mm) with inclusion I (10 mm in diameter), where the inclusion I is located at (X = 140 mm, Y = 50 mm, Z = 10 mm). Figure 8 shows the reconstructed image (modulus part) of the object. The inclusion is clearly visible in the image at the correct location.

Figure 9 shows the dielectric object consisting of external cube I (180 mm by 160 mm by 40 mm) and two inclusions of type I (10 mm and 15 mm in diameter), where the inclusions are located at

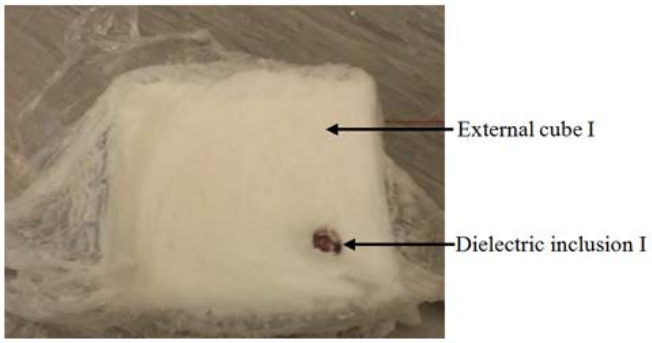

Figure 7. Photograph of the target object, including external cube I and one inclusion I.

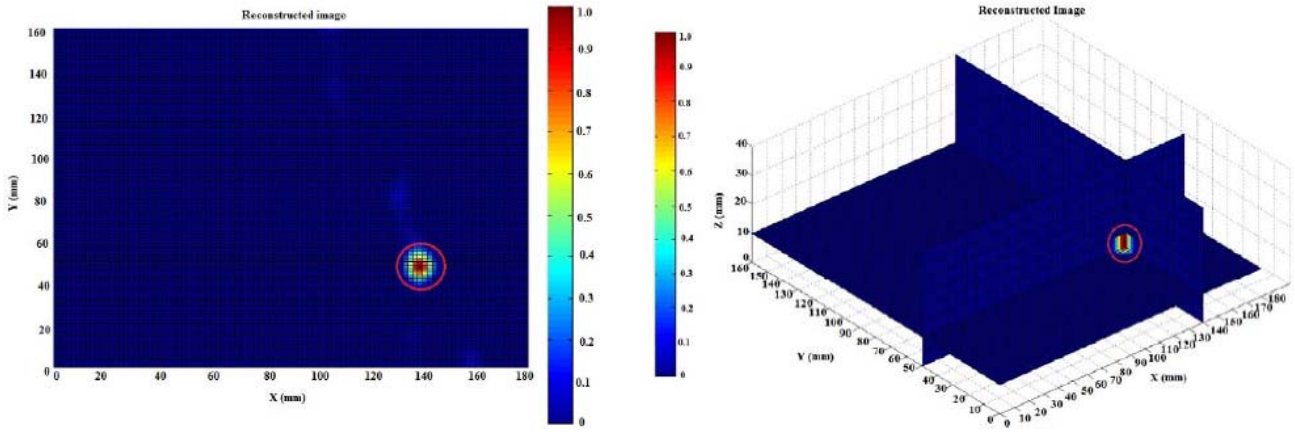

(a) (b)

Figure 8. (a) Top view. (b) Side view of 3-D image of one inclusion I.

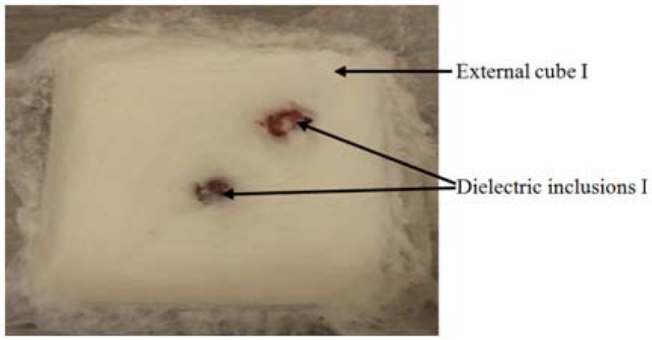

Figure 9. Photograph of the cube including external cube I and two inclusions I.

($X_1 = 95\,\text{mm}$, $Y_1 = 95\,\text{mm}$, $Z_1 = 25\,\text{mm}$) and ($X_2 = 138\,\text{mm}$, $Y_2 = 40\,\text{mm}$, $Z_2 = 25\,\text{mm}$). The distance between two inclusions is approximately 69.8 mm (2.9λ). Figure 10(a) shows a single 2-D slice of the reconstructed 3-D image and Figure 10(b) displays the 3-D reconstructed image (modulus part) of the dielectric object. It clearly shows two inclusions in the reconstructed 3-D image at the correct locations.

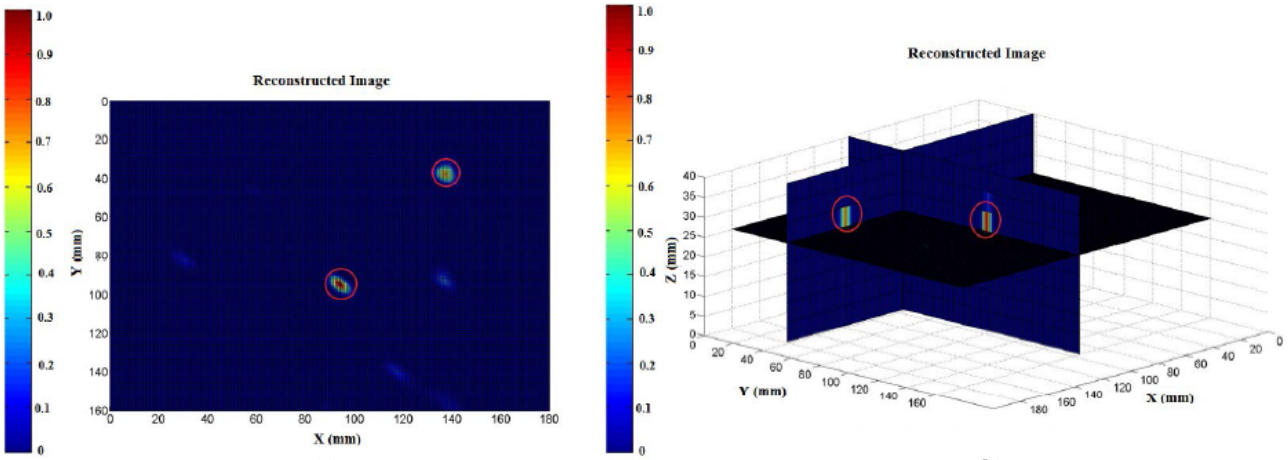

Figure 10. 3-D images with two inclusions I. (a) Top view. (b) Side view.

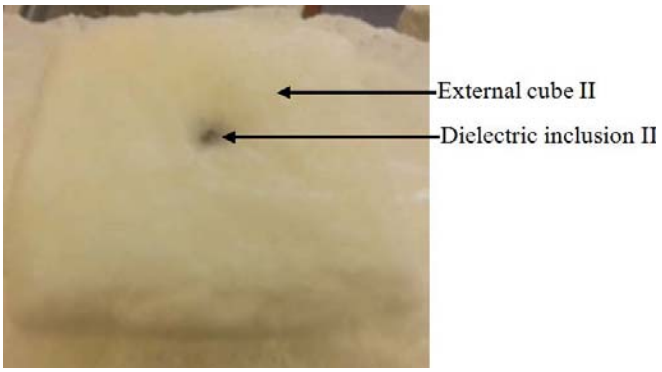

Figure 11. Photograph of the dielectric object, including cube II and one inclusion of type II (9 mm in diameter).

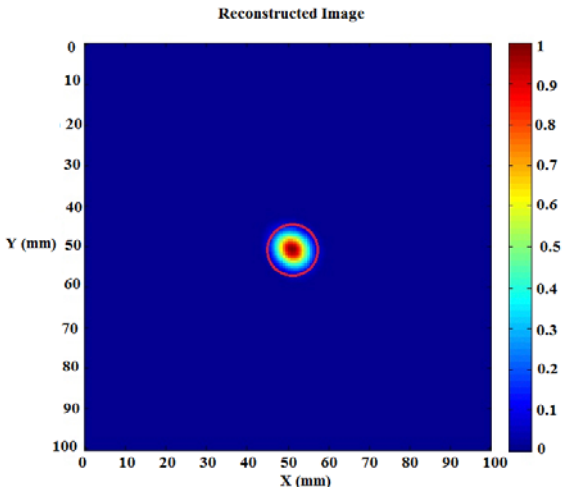

Figure 12. 2-D slice taken from 3-D image showing single inclusion of type II.

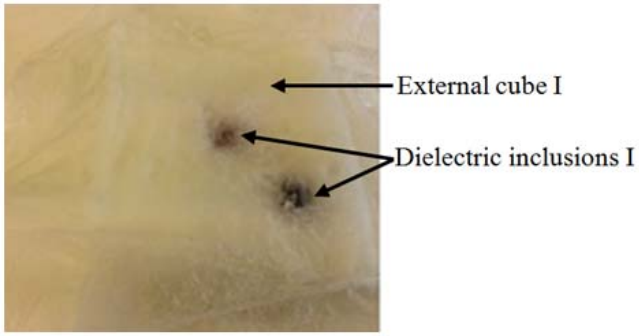

Figure 13. Photograph of the cube I including two inclusions of type I.

Figure 11 shows a dielectric object consisting of external cube II (100 mm by 100 mm by 40 mm) and one inclusion of type II (9 mm in diameter) where the inclusion is located at ($X = 50$ mm, $Y = 50$ mm, $Z = 35$ mm). Figure 12 shows a single 2-D slice of the reconstructed 3-D dielectric object.

Colour bars in Figure 8 and Figure 10 plot signal energy on a linear scale, normalized to the maximum in the volume. Values below 0.1 are rendered as blue.

5.2. Quantitative Reconstruction

Figure 13 shows the dielectric object (100 mm by 100 mm by 30 mm) including an external cube I and two inclusions of type I (10 mm in diameter), where the inclusions are located at ($X_1 = 50$ mm, $Y_1 = 50$ mm, $Z_1 = 20$ mm) and ($X_2 = 70$ mm, $Y_2 = 80$ mm, $Z_2 = 20$ mm).

The 2-D reconstructed images (modulus part) of a dielectric object at frequencies ranging from 10

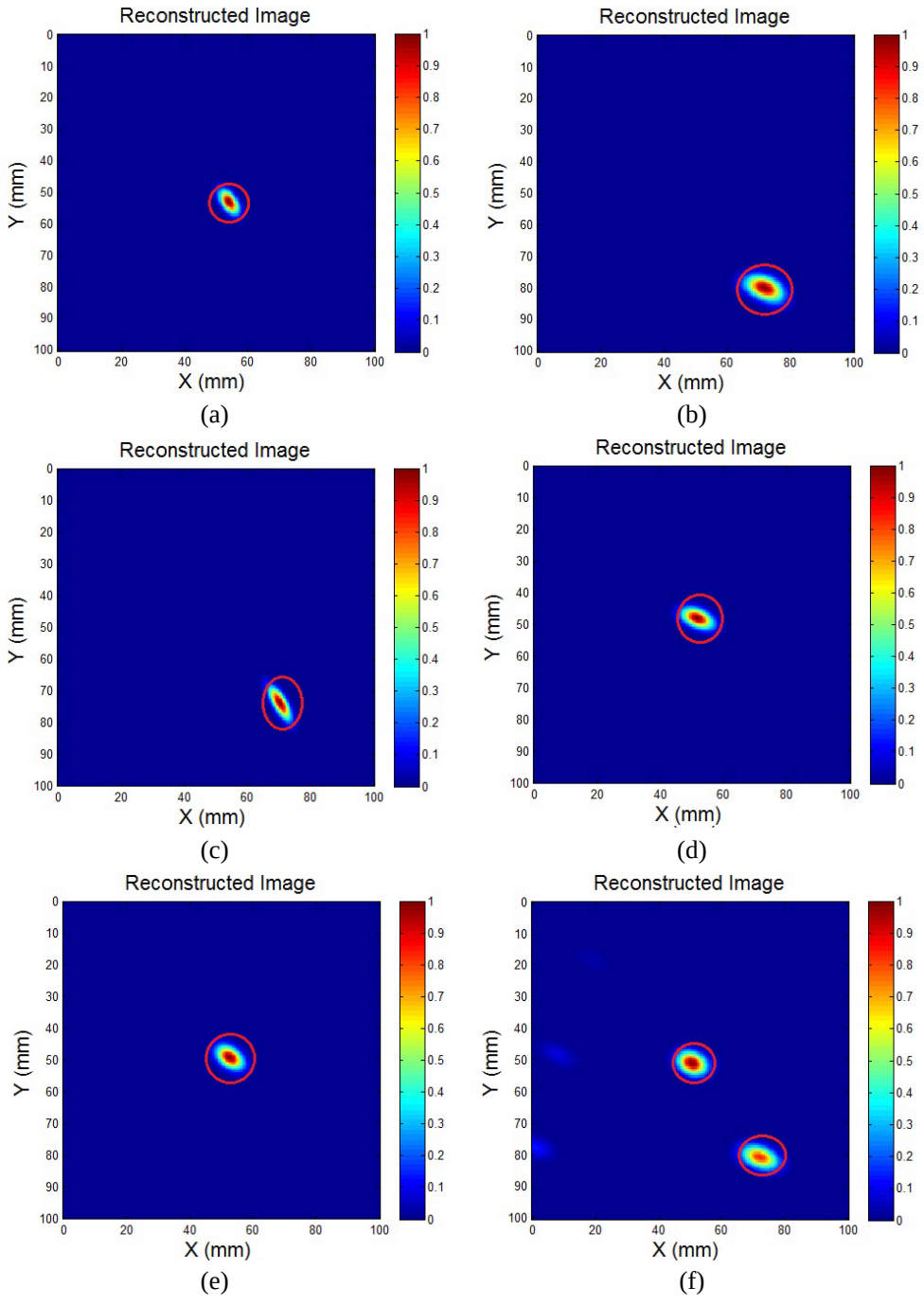

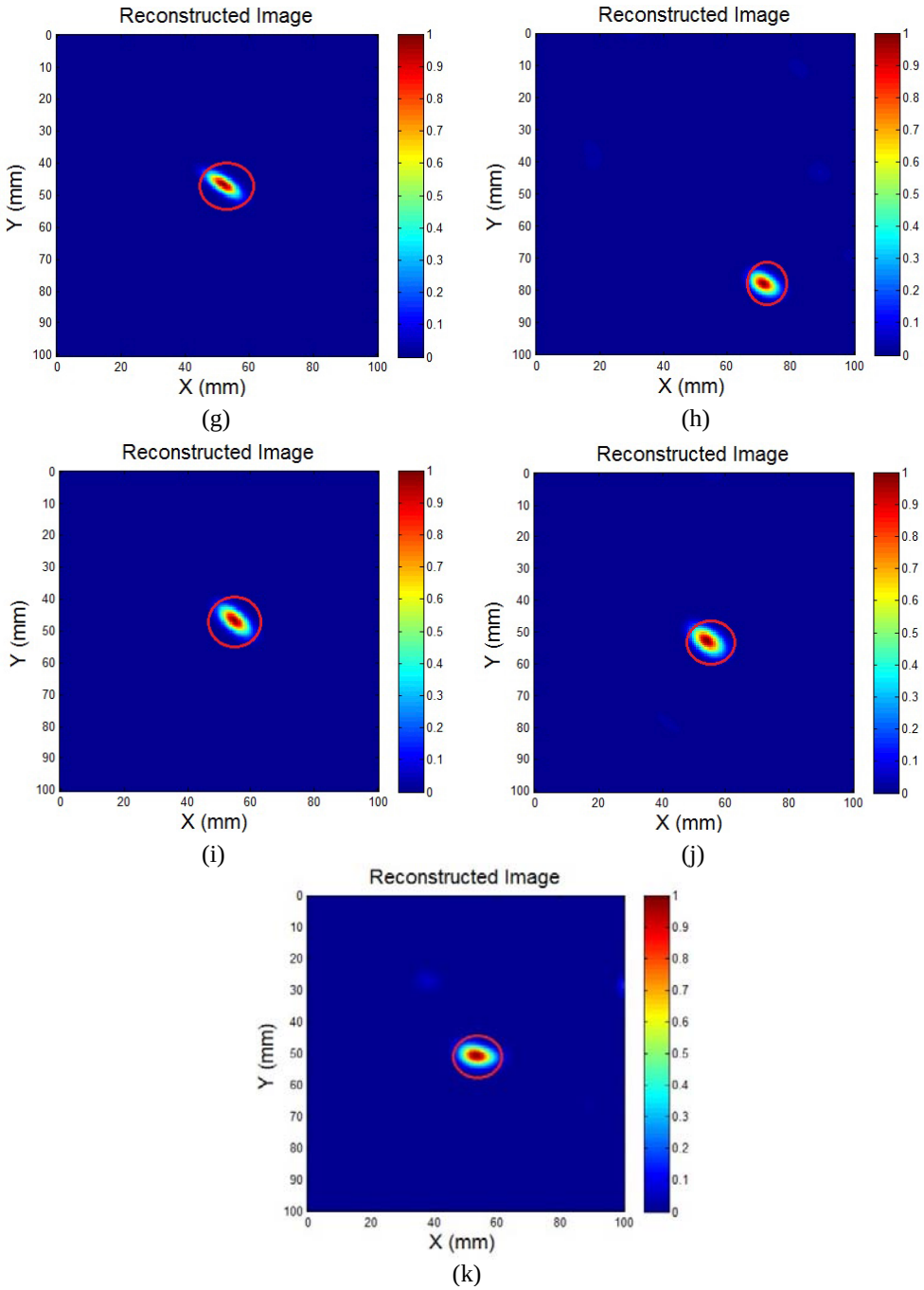

Figure 14. Reconstructed images of two inclusions I at a frequency. (a) 10 GHz. (b) 11 GHz. (c) 12 GHz. (d) 12.2 GHz. (e) 12.4 GHz. (f) 12.6 GHz. (g) 12.8 GHz. (h) 13 GHz. (i) 14 GHz. (j) 15 GHz. (k) 16 GHz.

to 16 GHz are represented in Figure 14. Results indicate that two inclusions are detected more clearly within the reconstructed image when the operating frequency is carried out at 12.6 GHz. As can be seen that only one inclusion is represented in the reconstruction image when the operating frequency range spans from 10 to 16 GHz, but not 12.6 GHz. It seems like the operating frequency of 12.6 GHz provides better quality of the image, sensitivity, and space resolution.

Figure 15 and Figure 16 demonstrate the real part and imaginary part of the reconstructed images that obtained at frequency of 12.6 GHz with different numbers of retina elements respectively, the original image as shown in Figure 7. It can be seen that the number of elements have a significant effect

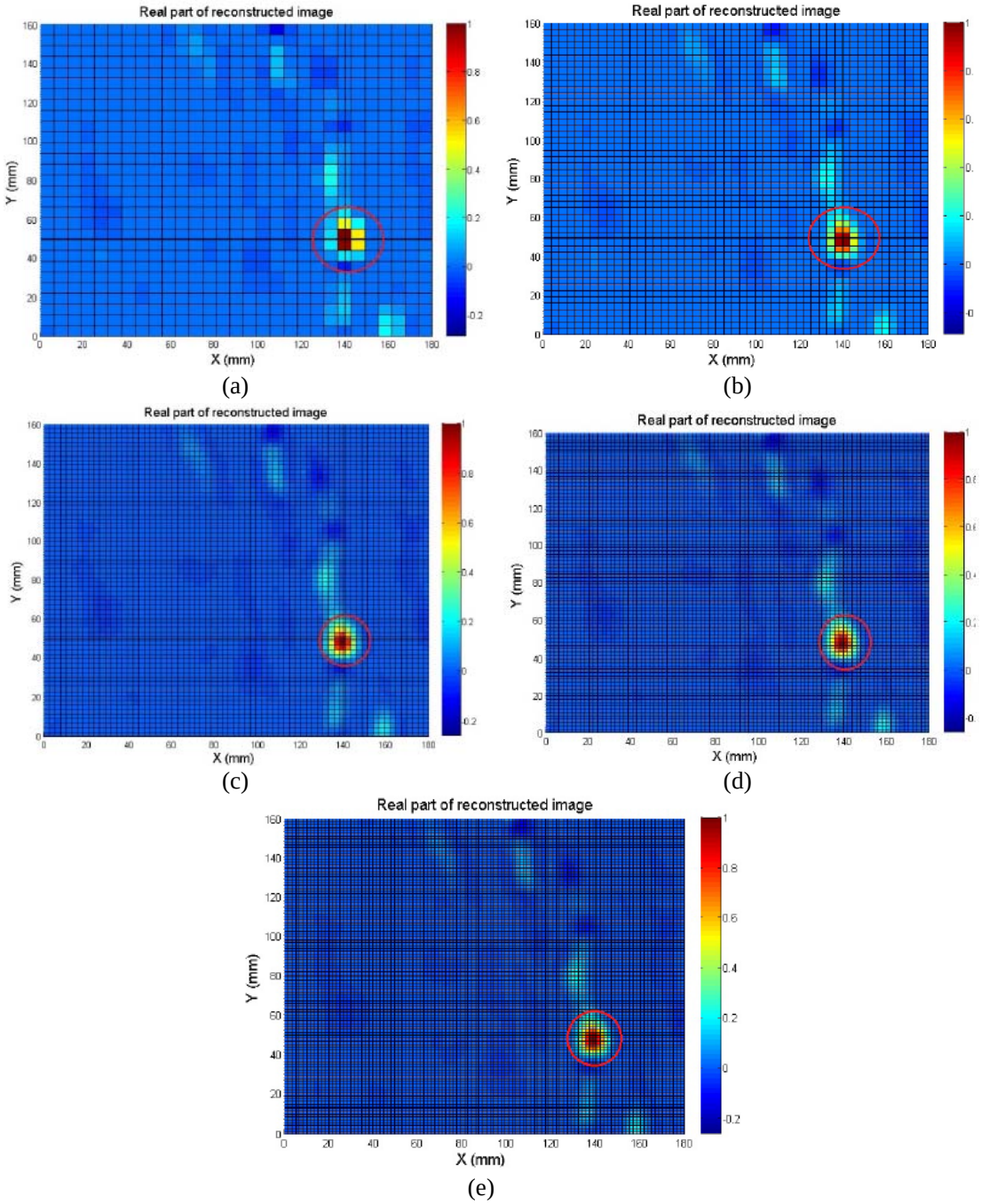

Figure 15. Side view of real part of reconstructed image with one inclusion. (a) 30 by 30 by 9 data. (b) 50 by 50 by 9 data. (c) 70 by 70 by 9 data. (d) 90 by 90 by 9 data. (e) 110 by 110 by 9 data.

on the quality of the image. Moreover, the detection of the inclusion comes mainly from the distribution of the real part.

Colour bars in Figures 14–16 plot signal energy on a linear scale, normalized to the maximum in the volume. Values below 0.1 are rendered as blue.

5.3. Discussion

The data collection time was approximately 10 minutes for 15 receivers at one selected height, while the CPU time required to produce a 2-D image was approximately 0.5 seconds on an Intel Core (TM) i5

3 : 2 GHz with 8 GB RAM. The time required to measure 15 receivers at 10 different heights was approximately 100 minutes, while the CPU time required to produce a 3-D image was approximately 1 minute on an Intel Core (TM) i5 3 : 2 GHz with 8 GB RAM.

The artefacts are presented in some experimental results, especially in the real and imaginary part of the reconstructed image. In general, they are due to the measurement noise caused by the environment, the equipment setups and experimental performance of the antennas.

The image resolution of the HMI image technique depends highly on the antenna baseline difference, in other words, the antenna locations on a 2-D array plane as presented in Equation (4). Achieved results (see Figure 15 and Figure 16) suggest that the number of elements have a significant effect on the quality

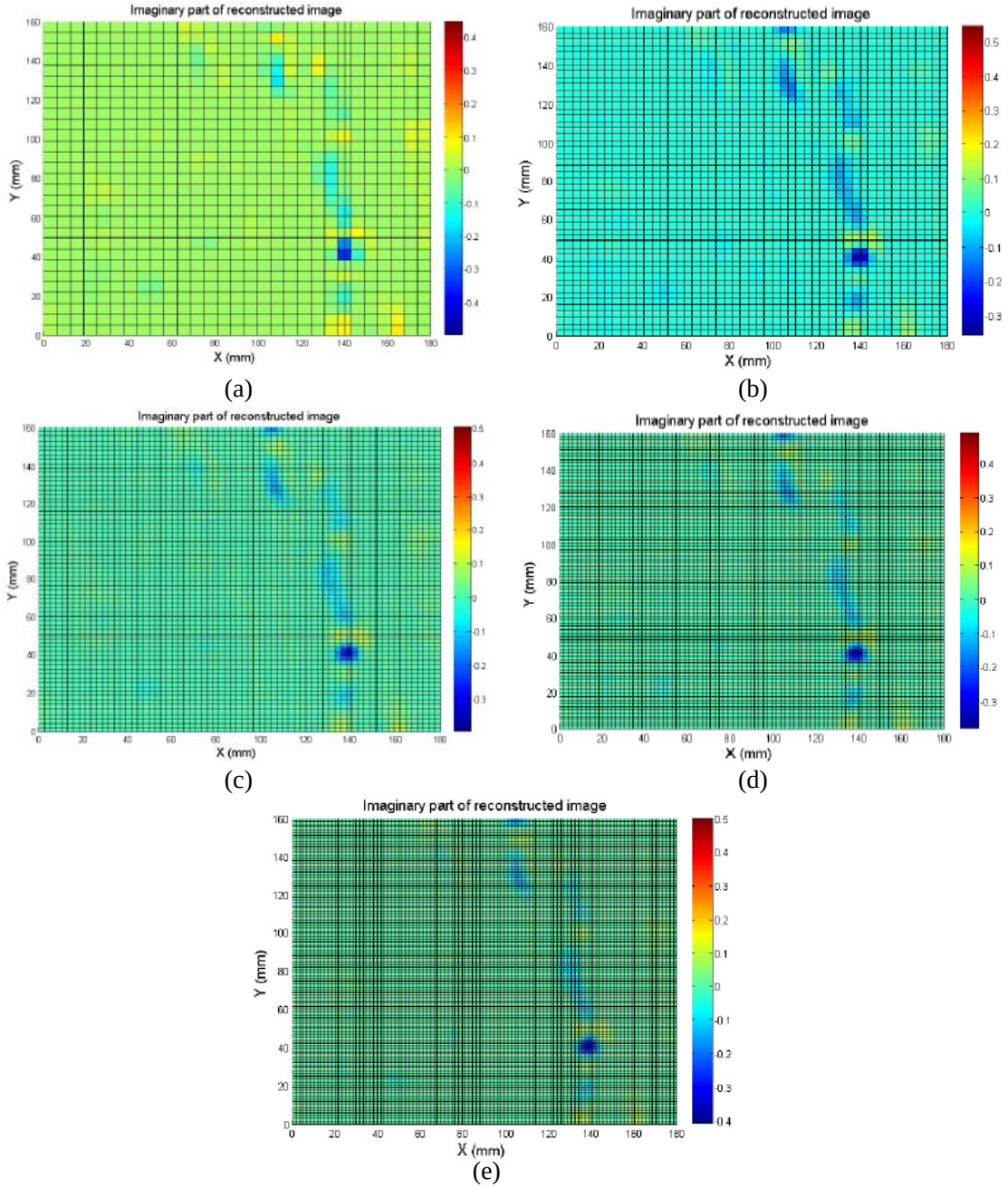

Figure 16. Side view of the imaginary part of the reconstructed image with one inclusion. (a) 30 by 30 by 9 data. (b) 50 by 50 by 9 data. (c) 70 by 70 by 9 data. (d) 90 by 90 by 9 data. (e) 110 by 110 by 9 data.

of the image. Moreover, the detection of the inclusion comes mainly from the distribution of the real part of the reconstructed image. More details of both experimental and numerical investigation of antenna array configurations to produce high-resolution images using small numbers of antennas are presented in [36]. Our previous studies [36] have demonstrated that in real measurement environment, the scale product of 2-D image $\tilde{I}_{Z_n}$ and antenna array configurations are helpful to reduce measurement noise.

The major limitation of the simplified HMI system is that a long operation time was required to generate a good quality 3-D image. For example, the data collection time was approximately 500 minutes for 15 receivers at 49 selected heights, and the CPU time required to calculate a 3-D image (data collected at 49 different heights) was approximately 2 minutes on an Intel Xeon E5620 2 : 4 GHz with 18 GB RAM. This was caused mainly due to manual operation and manual height adjustment of the antenna array plane. However, this limitation can be overcome in the future by developing a complex practical system to collect and store data automatically. In [36], we have investigated the penetration depth, operating frequency range, antenna, antenna array configurations, the best distance between the antenna array and the imaged object. More simulation results of dielectric objects that used the published dielectric properties of human breasts are detailed in [37], the contrast between breast lesion, fat tissue, gland and skin is very close to the real breast. Due to this major limitation of the simplified HMI system, only few experimental results are presented in this paper.

The far-field HMI technique is very different from various existing near-field microwave holography techniques [18–21]:

(1) The far-field HMI technique uses physical displacement (scan of the distance) between the antenna array plane and the imaged object over a specified range (vertical) to obtain depth information from sequenced 2-D images, which is very different from holography system in [18, 19] that is fixed along a range and uses ultra-wideband information to attain depth resolution. Furthermore, the scattered field formulation used in our paper is subject to a far-field approximation but not subject to a linear-Born approximation. In contrast [18, 19], the 2-D reconstruction algorithms in [18, 19] rely on the linear-Born model of the scattered field to deduce a Fourier-transform relationship between the image intensity and the permittivity distribution of the imaged object.

(2) An indirect holographic technique reported in [18, 19] is more typical at optical frequencies, which is very different from our proposed technique. Additionally, only single media object was presented in [18, 19]. Our achieved experimental results suggest that the proposed technique has the ability to produce a 3-D image of multimedia dielectric object and detect small inclusions embedded within an object. The invention has potential application to tissue imaging. Experimental evaluation of the HMI technique in biological tissues and real breasts is currently undergoing project, results will be reported in the near future.

Compared to other microwave imaging techniques, the HMI technique has the following benefits:

(1) We did not need to explicitly determine the complex permittivity or total electric field to generate an image that contains information about the object's interior. The quantity that we reconstructed at each voxel is that defined as intensity function. Physically, this quantity is proportional to the squared modulus of the polarisation charge density at each point inside the object. Note that this is a scalar quantity, which simplifies the image reconstruction. The intensity function is simply a 'proxy' that is proportional to the squared modulus of the permittivity contrast.

(2) We can obtain 3-D images of reasonable resolution using data acquired at just one frequency. We do not need to use broadband systems and measurements like UWB radar methods.

(3) Another potential benefit of the methodology is that the liquid matching medium was not necessary in the measurement system. This allows for a lower cost and easier setup for the experimental system. However, this claim needs further substantiation when the system is used with real human tissue. It should be noted that the relative permittivity distribution models the inclusion and its immediate surrounding medium. The relative permittivity ε_1 is that of the (homogenous) ambient medium in which the entire object is immersed. In our case, the experiments were performed without a matching medium so $\varepsilon_1 = 1$ (air). If a matching medium was to be used then the value of ε_1 would need to be chosen accordingly. The scattered field formulation in our Equation (2) was written in this way to model the general case even though our experiments set $\varepsilon_1 = 1$.

(4) Additionally, the antenna array provides the maximum combination of receiving antennas and enables the collection of out of plane transmission data. For a single transmitter and 15 receivers, the total number of independent measurement points using the HMI technique is 210, but it is only 15 points for the same number of antennas using the microwave imaging approach detailed in [39]. This will significantly improve the image quality for a given number of antennas, whilst reducing the cost. A comparison of HMI results with other microwave imaging approaches are detailed in [36].

5.4. Future Works

Our intention was to demonstrate the fact that a 3-D image can be generated from a series of 2-D projection data obtained using the interferometric approach. We also intended to report on initial experimental findings to demonstrate that our technique is novel and has potential to warrant further investigation. Implementing the 3-D HMI technique on real biological tissues is undergoing project, results will be reported in the near future. The potential applications of this technique are most likely breast cancer detection, and brain stroke detection. An important issue that will need to be addressed in the future is the extension of the analysis to 3-D phantoms with a realistic shape and realistic tissue architecture. In the case of breast cancer detection using the 3-D HMI technique, further areas of study including:

- Development of a complex practical system to significantly reduce the data acquisition time.
- Development of a realistic breast phantom that is close to real human tissue architecture.
- Further experiments on multiple realistic breast phantoms to investigate the performance of breast cancer detection using HMI algorithms.
- Design and build a compact patch antenna array suitable for a clinical trial system setup.
- Validation of the 3-D HMI technique through measurement studies on living tissues and mastectomy tissue.
- Comparison between HMI images and other microwave images, as well as existing medical imaging tools such as X-ray mammography and MRI.
- Experimental investigation of image resolution using the complex practical system.

6. CONCLUSIONS

We have investigated a new 3-D HMI technique for imaging dielectric object theoretically and experimentally. In this paper, we report our preliminary analysis and development of 3-D HMI system to generate a microwave image. The technique uses physical displacement between the antenna array plane and the imaged object over a specified range in order to obtain depth information from sequence 2-D images. Experimental investigation of multimedia dielectric objects with different dielectric properties (contrast), sizes and locations is presented. Experimental results show that the proposed technique has the ability to produce good quality images of dielectric objects and detect small inclusions within the object.

A matching medium was not required in this preliminary experiment, only air, which greatly simplified the practical implementation of such a system and reduced the associated cost. We claim that our proposed technique has the potential to be implemented without a matching medium. However, this claim needs further substantiation when the system is used with real human tissue.

The future work will focus on developing realistic breast phantoms and clinical suitable system, measurements on realistic breast phantoms, biological tissues as well as real breasts to validate that the proposed technique has a potential for imaging biological tissues.

REFERENCES

1. Manickavasagan, A. and H. Jayasuriya, "Imaging with electromagnetic spectrum," *Applications in Food and Agriculture*, 108, Springer, Heidelberg, New York, Dordrecht, London, 2014.

2. Jofre, L., M. S. Hawley, A. Broquetas, E. de Los Reyes, M. Ferrando, and A. R. Elias-Fuste, "Medical imaging with a microwave tomographic scanner," *IEEE Trans. on Biomedical Engineering*, Vol. 37, No. 3, 303–312, 1990.
3. Mehta, P., K. Chand, D. Narayanswamy, D. G. Beetner, R. Zoughi, and W. V. Stoecker, "Microwave reflectometry as a novel diagnostic tool for detection of skin cancers," *IEEE Trans. on Instrumentation and Measurement*, Vol. 55, No. 4, 1309–1316, 2006.
4. Sheen, D. M., D. L. McMakin, and T. E. Hall, "Three-dimensional millimeter-wave imaging for concealed weapon detection," *IEEE Trans. on Microwave Theory and Techniques*, Vol. 49, No. 9, 1581–1592, 2001.
5. Fear, E. C., S. C. Hagness, P. M. Meaney, M. Okoniewski, and M. A. Stuchly, "Enhancing breast tumor detection with near-field imaging," *IEEE Microwave Magazine*, Vol. 3, No. 1, 48–56, 2002.
6. Li, X., E. J. Bond, B. D. Van Veen, and S. C. Hagness, "An overview of ultra-wideband microwave imaging via space-time beamforming for early-stage breast-cancer detection," *IEEE Antennas and Propagation Magazine*, Vol. 47, No. 1, 19–34, 2005.
7. Sill, J. M. and E. C. Fear, "Tissue sensing adaptive radar for breast cancer detection-experimental investigation of simple tumor models," *IEEE Trans. on Microwave Theory and Techniques*, Vol. 53, No. 11, 3312–3319, 2005.
8. Xie, Y., B. Guo, L. Xu, J. Li, and P. Stoica, "Multistatic adaptive microwave imaging for early breast cancer detection," *IEEE Trans. on Biomedical Engineering*, Vol. 53, No. 8, 1647–1657, 2005.
9. Davis, S. K., H. Tandradinata, S. C. Hagness, and B. D. Van Veen, "Ultrawideband microwave breast cancer detection: A detection-theoretic approach using the generalized likelihood ratio test," *IEEE Trans. on Biomedical Engineering*, Vol. 52, No. 7, 1237–1250, 2005.
10. Hassan, A. M. and E. L. Shenawee, "Review of electromagnetic techniques for breast cancer detection," *IEEE Reviews in Biomedical Engineering*, Vol. 4, 103–118, 2011.
11. Klemm, M., I. J. Craddock, J. A. Leendertz, A. Preece, and R. Benjamin, "Radar-based breast cancer detection using a hemispherical antenna array — Experimental results," *IEEE Trans. on Antennas and Propagation*, Vol. 57, No. 6, 1692–1704, 2009.
12. Klemm, M., J. Leendertz, D. Gibbins, I. J. Craddock, A. Preece, and R. Benjamin, "Microwave radar-based differential breast cancer imaging: Imaging in homogeneous breast phantoms and low contrast scenarios," *IEEE Trans. on Antennas and Propagation*, Vol. 58, No. 7, 2337–2344, 2010.
13. Fang, Q., P. M. Meaney, S. D. Geimer, A. V. Streltsov, and K. D. Paulsen, "Microwave image reconstruction from 3-D fields coupled to 2-D parameter estimation," *IEEE Trans. on Medical Imaging*, Vol. 23, No. 4, 475–484, 2004.
14. Rubæk, T., O. S. Kim, and P. Meincke, "Computational validation of a 3-D microwave imaging system for breast-cancer screening," *IEEE Trans. on Antennas and Propagation*, Vol. 57, No. 7, 2105–2115, 2009.
15. Fear, E. C., "Microwave imaging of the breast," *Technology in Cancer Research & Treatment*, Vol. 4, No. 1, 69–82, 2005.
16. Tipa, R. and O. Baltag, "Microwave thermography for cancer detection," *Romanian Journal of Physics*, Vol. 51, Nos. 3–4, 371, 2006.
17. Grzegorczyk, T. M., P. M. Meaney, P. A. Kaufman, P. M. di Florio-Alexander, and K. D. Paulsen, "Fast 3-D tomographic microwave imaging for breast cancer detection," *IEEE Trans. on Medical Imaging*, Vol. 31, No. 8, 1584–1592, 2012.
18. Smith, D., M. Leach, M. Elsdon, and S. J. Foti, "Indirect holographic techniques for determining antenna radiation characteristics and imaging aperture fields," *IEEE Antennas and Propagation Magazine*, Vol. 49, No. 1, 54–67, 2007.
19. Jayanthy, M., N. Selvanathan, M. Abu-Bakar, D. Smith, H. M. Elgabroun, P. M. Yeong, and S. S. Kumar, "Microwave holographic imaging technique for tumour detection," *3rd Kuala Lumpur International Conference on Biomedical Engineering*, 275–277, 2006.
20. Ravan, M., R. K. Amineh, and N. K. Nikolova, "Two-dimensional near-field microwave holography," *Inverse Problems*, Vol. 26, No. 5, 055011, 2010.

21. Amineh, R. K., M. Ravan, A. Khalatpour, and N. K. Nikolova, "Three-dimensional near-field microwave holography using reflected and transmitted signals," *IEEE Trans. on Antennas and Propagation*, Vol. 59, No. 12, 4777–4789, 2011.
22. Meaney, P. M., M. W. Fanning, T. Raynolds, C. J. Fox, Q. Fang, C. A. Kogel, and K. D. Paulsen, "Initial clinical experience with microwave breast imaging in women with normal mammography," *Academic Radiology*, Vol. 14, No. 2, 207–218, 2007.
23. Farhat, N. H., "Microwave holography and coherent tomography," *Medical Applications of Microwave Imaging*, 66–81, 1986.
24. Chaudhary, S. S., R. K. Mishra, A. Swarup, and J. M. Thomas, "Dielectric properties of normal and malignant human breast tissues at radiowave and microwave frequencies," *Indian J. Biochem., Biophys.*, Vol. 21, 76–79, 1984.
25. Joines, W. T., Y. Zhang, C. Li, and R. L. Jirtle, "The measured electrical properties of normal and malignant human tissues from 50 to 900 MHz," *Medical Physics*, Vol. 21, No. 4, 547, 1994.
26. Gabriel, C., S. Gabriel, and E. Corthout, "The dielectric properties of biological tissues: I. Literature survey," *Physics in Medicine and Biology*, Vol. 41, No. 11, 2231, 1991.
27. Gabriel, S., R. W. Lau, and C. Gabriel, "The dielectric properties of biological tissues: II. Measurements in the frequency range 10 Hz to 20 GHz," *Physics in Medicine and Biology*, Vol. 41, No. 11, 2251, 1999.
28. Lazebnik, M., D. Popovic, L. McCartney, C. B. Watkins, M. J. Lindstrom, J. Harter, and S. C. Hagness, "A large-scale study of the ultrawideband microwave dielectric properties of normal, benign and malignant breast tissues obtained from cancer surgeries," *Physics in Medicine and Biology*, Vol. 52, No. 20, 2637, 2007.
29. Abbosh, A., "Early breast cancer detection using hybrid imaging modality," *Antennas and Propagation Society International Symposium*, 1–4, 2009.
30. Wang, L., A. M. Al-Jumaily, and R. Simpkin, "Holographic microwave imaging array for brain stroke detection," *Journal of Signal and Information Processing*, Vol. 4, No. 3B, 96–101, 2013.
31. Wang, L., R. Simpkin, and A. M. Al-Jumaily, "Holographic microwave imaging for medical applications," *Journal of Biomedical Science and Engineering*, Vol. 6, 823–833, 2013.
32. Wang, L., R. Simpkin, and A. M. Al-Jumaily, "Holographic microwave imaging array for early breast cancer detection," *2012 ASME International Mechanical Engineering Congress and Exposition*, 45–51, 2012.
33. Wang, L., R. Simpkin, and A. M. Al-Jumaily, "3D breast cancer imaging using holographic microwave interferometry," *Proceedings of the 27th Conference on Image and Vision Computing*, 180–185, ACM, New Zealand, 2012.
34. Wang, L., R. Simpkin, and A. M. Al-Jumaily, "Holographic microwave imaging array: Experimental investigation of breast tumour detection," *2013 IEEE International Workshop on Electromagnetics (iWEM)*, 61–64, 2013.
35. Wang, L., R. Simpkin, and A. M. Al-Jumaily, "Open-ended waveguide antenna for microwave breast cancer detection," *2013 IEEE International Workshop on Electromagnetics (iWEM)*, 65–68, 2013.
36. Wang, L., "Holographic microwave imaging for lesion detection," Doctoral Dissertation, Auckland University of Technology, 2013.
37. Wang, L., A. M. Al-Jumaily, and R. Simpkin, "Imaging of 3-D dielectric objects using far-field holographic microwave imaging technique," *Progress In Electromagnetics Research B*, 2014.
38. Levanda, R. and A. Leshem, "Synthetic aperture radio telescopes," *IEEE Signal Processing Magazine*, Vol. 27, No. 1, 14–29, 2010.
39. Simonov, N., S. I. Jeon, S. H. Son, J. M. Lee, and H. J. Kim, "3D microwave breast imaging based on multistatic radar concept system," *Journal of the Korean Institute of Electromagnetic Engineering and Science*, Vol. 12, No. 1, 107–114, 2012.